PHYSICAL REVIEW D **84,** 072001 (2011)

First search for atmospheric and extraterrestrial neutrino-induced cascades with the IceCube detector

R. Abbasi,[28] Y. Abdou,[22] T. Abu-Zayyad,[33] J. Adams,[16] J. A. Aguilar,[28] M. Ahlers,[32] K. Andeen,[28] J. Auffenberg,[38] X. Bai,[31] M. Baker,[28] S. W. Barwick,[24] R. Bay,[7] J. L. Bazo Alba,[39] K. Beattie,[8] J. J. Beatty,[18,19] S. Bechet,[13] J. K. Becker,[10] K.-H. Becker,[38] M. L. Benabderrahmane,[39] S. BenZvi,[28] J. Berdermann,[39] P. Berghaus,[28] D. Berley,[17] E. Bernardini,[39] D. Bertrand,[13] D. Z. Besson,[26] D. Bindig,[38] M. Bissok,[1] E. Blaufuss,[17] J. Blumenthal,[1] D. J. Boersma,[1] C. Bohm,[34] D. Bose,[14] S. Böser,[11] O. Botner,[37] J. Braun,[28] A. M. Brown,[16] S. Buitink,[8] M. Carson,[22] D. Chirkin,[28] B. Christy,[17] J. Clem,[31] F. Clevermann,[20] S. Cohen,[25] C. Colnard,[23] D. F. Cowen,[36,35] M. V. D'Agostino,[7] M. Danninger,[34] J. Daughhetee,[5] J. C. Davis,[18] C. De Clercq,[14] L. Demirörs,[25] O. Depaepe,[14] F. Descamps,[22] P. Desiati,[28] G. de Vries-Uiterweerd,[22] T. DeYoung,[36] J. C. Díaz-Vélez,[28] M. Dierckxsens,[13] J. Dreyer,[10] J. P. Dumm,[28] R. Ehrlich,[17] J. Eisch,[28] R. W. Ellsworth,[17] O. Engdegård,[37] S. Euler,[1] P. A. Evenson,[31] O. Fadiran,[4] A. R. Fazely,[6] A. Fedynitch,[10] T. Feusels,[22] K. Filimonov,[7] C. Finley,[34] T. Fischer-Wasels,[38] M. M. Foerster,[36] B. D. Fox,[36] A. Franckowiak,[11] R. Franke,[39] T. K. Gaisser,[31] J. Gallagher,[27] M. Geisler,[1] L. Gerhardt,[8,7] L. Gladstone,[28] T. Glüsenkamp,[1] A. Goldschmidt,[8] J. A. Goodman,[17] D. Grant,[21] T. Griesel,[29] A. Groß,[16,23] S. Grullon,[28] M. Gurtner,[38] C. Ha,[36] A. Hallgren,[37] F. Halzen,[28] K. Han,[16] K. Hanson,[13,28] D. Heinen,[1] K. Helbing,[38] P. Herquet,[30] S. Hickford,[16] G. C. Hill,[28] K. D. Hoffman,[17] A. Homeier,[11] K. Hoshina,[28] D. Hubert,[14] W. Huelsnitz,[17] J.-P. Hülß,[1] P. O. Hulth,[34] K. Hultqvist,[34] S. Hussain,[31] A. Ishihara,[15] J. Jacobsen,[28] G. S. Japaridze,[4] H. Johansson,[34] J. M. Joseph,[8] K.-H. Kampert,[38] A. Kappes,[9] T. Karg,[38] A. Karle,[28] J. L. Kelley,[28] N. Kemming,[9] P. Kenny,[26] J. Kiryluk,[8,7,*] F. Kislat,[39] S. R. Klein,[8,7] J.-H. Köhne,[20] G. Kohnen,[30] H. Kolanoski,[9] L. Köpke,[29] S. Kopper,[38] D. J. Koskinen,[36] M. Kowalski,[11] T. Kowarik,[29] M. Krasberg,[28] T. Krings,[1] G. Kroll,[29] K. Kuehn,[18] T. Kuwabara,[31] M. Labare,[14] S. Lafebre,[36] K. Laihem,[1] H. Landsman,[28] M. J. Larson,[36] R. Lauer,[39] R. Lehmann,[9] J. Lünemann,[29] J. Madsen,[33] P. Majumdar,[39] A. Marotta,[13] R. Maruyama,[28] K. Mase,[15] H. S. Matis,[8] K. Meagher,[17] M. Merck,[28] P. Mészáros,[35,36] T. Meures,[1] E. Middell,[39] N. Milke,[20] J. Miller,[37] T. Montaruli,[28,†] R. Morse,[28] S. M. Movit,[35] R. Nahnhauer,[39] J. W. Nam,[24] U. Naumann,[38] P. Nießen,[31] D. R. Nygren,[8] S. Odrowski,[23] A. Olivas,[17] M. Olivo,[37,10] A. O'Murchadha,[28] M. Ono,[15] S. Panknin,[11] L. Paul,[1] C. Pérez de los Heros,[37] J. Petrovic,[13] A. Piegsa,[29] D. Pieloth,[20] R. Porrata,[7] J. Posselt,[38] P. B. Price,[7] M. Prikockis,[36] G. T. Przybylski,[8] K. Rawlins,[3] P. Redl,[17] E. Resconi,[23] W. Rhode,[20] M. Ribordy,[25] A. Rizzo,[14] J. P. Rodrigues,[28] P. Roth,[17] F. Rothmaier,[29] C. Rott,[18] T. Ruhe,[20] D. Rutledge,[36] B. Ruzybayev,[31] D. Ryckbosch,[22] H.-G. Sander,[29] M. Santander,[28] S. Sarkar,[32] K. Schatto,[29] T. Schmidt,[17] A. Schoenwald,[39] A. Schukraft,[1] A. Schultes,[38] O. Schulz,[23] M. Schunck,[1] D. Seckel,[31] B. Semburg,[38] S. H. Seo,[34] Y. Sestayo,[23] S. Seunarine,[12] A. Silvestri,[24] A. Slipak,[36] G. M. Spiczak,[33] C. Spiering,[39] M. Stamatikos,[18,‡] T. Stanev,[31] G. Stephens,[36] T. Stezelberger,[8] R. G. Stokstad,[8] S. Stoyanov,[31] E. A. Strahler,[14] T. Straszheim,[17] G. W. Sullivan,[17] Q. Swillens,[13] H. Taavola,[37] I. Taboada,[5] A. Tamburro,[33] O. Tarasova,[39] A. Tepe,[5] S. Ter-Antonyan,[6] S. Tilav,[31] P. A. Toale,[36] S. Toscano,[28] D. Tosi,[39] D. Turčan,[17] N. van Eijndhoven,[14] J. Vandenbroucke,[7] A. Van Overloop,[22] J. van Santen,[28] M. Vehring,[1] M. Voge,[23] B. Voigt,[39] C. Walck,[34] T. Waldenmaier,[9] M. Wallraff,[1] M. Walter,[39] Ch. Weaver,[28] C. Wendt,[28] S. Westerhoff,[28] N. Whitehorn,[28] K. Wiebe,[29] C. H. Wiebusch,[1] D. R. Williams,[2] R. Wischnewski,[39] H. Wissing,[17] M. Wolf,[23] K. Woschnagg,[7] C. Xu,[31] X. W. Xu,[6] G. Yodh,[24] S. Yoshida,[15] and P. Zarzhitsky[2]

(IceCube Collaboration)

[1]*III. Physikalisches Institut, RWTH Aachen University, D-52056 Aachen, Germany*
[2]*Department of Physics and Astronomy, University of Alabama, Tuscaloosa, Alabama 35487, USA*
[3]*Department of Physics and Astronomy, University of Alaska Anchorage, 3211 Providence Dr., Anchorage, Alaska 99508, USA*
[4]*CTSPS, Clark-Atlanta University, Atlanta, Georgia 30314, USA*
[5]*School of Physics and Center for Relativistic Astrophysics, Georgia Institute of Technology, Atlanta, Georgia 30332, USA*
[6]*Department of Physics, Southern University, Baton Rouge, Louisiana 70813, USA*
[7]*Department of Physics, University of California, Berkeley, California 94720, USA*
[8]*Lawrence Berkeley National Laboratory, Berkeley, California 94720, USA*
[9]*Institut für Physik, Humboldt-Universität zu Berlin, D-12489 Berlin, Germany*
[10]*Fakultät für Physik & Astronomie, Ruhr-Universität Bochum, D-44780 Bochum, Germany*
[11]*Physikalisches Institut, Universität Bonn, Nussallee 12, D-53115 Bonn, Germany*
[12]*Department of Physics, University of the West Indies, Cave Hill Campus, Bridgetown BB11000, Barbados*
[13]*Université Libre de Bruxelles, Science Faculty CP230, B-1050 Brussels, Belgium*

1550-7998/2011/84(7)/072001(15)

[14]*Vrije Universiteit Brussel, Dienst ELEM, B-1050 Brussels, Belgium*
[15]*Department of Physics, Chiba University, Chiba 263-8522, Japan*
[16]*Department of Physics and Astronomy, University of Canterbury, Private Bag 4800, Christchurch, New Zealand*
[17]*Department of Physics, University of Maryland, College Park, Maryland 20742, USA*
[18]*Department of Physics and Center for Cosmology and Astro-Particle Physics, Ohio State University, Columbus, Ohio 43210, USA*
[19]*Department of Astronomy, Ohio State University, Columbus, Ohio 43210, USA*
[20]*Department of Physics, TU Dortmund University, D-44221 Dortmund, Germany*
[21]*Department of Physics, University of Alberta, Edmonton, Alberta, Canada T6G 2G7*
[22]*Department of Subatomic and Radiation Physics, University of Gent, B-9000 Gent, Belgium*
[23]*Max-Planck-Institut für Kernphysik, D-69177 Heidelberg, Germany*
[24]*Department of Physics and Astronomy, University of California, Irvine, California 92697, USA*
[25]*Laboratory for High Energy Physics, École Polytechnique Fédérale, CH-1015 Lausanne, Switzerland*
[26]*Department of Physics and Astronomy, University of Kansas, Lawrence, Kansas 66045, USA*
[27]*Department of Astronomy, University of Wisconsin, Madison, Wisconsin 53706, USA*
[28]*Department of Physics, University of Wisconsin, Madison, Wisconsin 53706, USA*
[29]*Institute of Physics, University of Mainz, Staudinger Weg 7, D-55099 Mainz, Germany*
[30]*Université de Mons, 7000 Mons, Belgium*
[31]*Bartol Research Institute and Department of Physics and Astronomy, University of Delaware, Newark, Delaware 19716, USA*
[32]*Department of Physics, University of Oxford, 1 Keble Road, Oxford OX1 3NP, UK*
[33]*Department of Physics, University of Wisconsin, River Falls, Wisconsin 54022, USA*
[34]*Oskar Klein Centre and Department of Physics, Stockholm University, SE-10691 Stockholm, Sweden*
[35]*Department of Astronomy and Astrophysics, Pennsylvania State University, University Park, Pennsylvania 16802, USA*
[36]*Department of Physics, Pennsylvania State University, University Park, Pennsylvania 16802, USA*
[37]*Department of Physics and Astronomy, Uppsala University, Box 516, S-75120 Uppsala, Sweden*
[38]*Department of Physics, University of Wuppertal, D-42119 Wuppertal, Germany*
[39]*DESY, D-15735 Zeuthen, Germany*

(Received 8 January 2011; published 3 October 2011)

We report on the first search for atmospheric and for diffuse astrophysical neutrino-induced showers (cascades) in the IceCube detector using 257 days of data collected in the year 2007–2008 with 22 strings active. A total of 14 events with energies above 16 TeV remained after event selections in the diffuse analysis, with an expected total background contribution of 8.3 ± 3.6. At 90% confidence we set an upper limit of $E^2\Phi_{90\%\text{CL}} < 3.6 \times 10^{-7}\ \text{GeV} \cdot \text{cm}^{-2} \cdot \text{s}^{-1} \cdot sr^{-1}$ on the diffuse flux of neutrinos of all flavors in the energy range between 24 TeV and 6.6 PeV assuming that $\Phi \propto E^{-2}$ and the flavor composition of the ν_e:ν_μ:ν_τ flux is 1:1:1 at the Earth. The atmospheric neutrino analysis was optimized for lower energies. A total of 12 events were observed with energies above 5 TeV. The observed number of events is consistent with the expected background, within the uncertainties.

DOI: 10.1103/PhysRevD.84.072001 PACS numbers: 14.60.Lm, 95.55.Vj, 95.85.Ry

I. INTRODUCTION

The origin of high-energy cosmic-rays is an area of active research in astrophysics. The sites where cosmic rays are accelerated are expected to produce high-energy neutrinos. Many types of objects, ranging from supernovae and gamma-ray bursters to active galactic nuclei [1], have been proposed as point sources of high-energy neutrinos and many searches for such sources have been made [2], yielding results consistent with background-only assumptions. If there are many point sources, each with an unobservably low flux, then the aggregate flux may still be observable as a diffuse flux.

Diffuse searches rely on the energy spectrum of the detected events to separate an extraterrestrial signal from atmospheric neutrinos produced in the interaction of cosmic rays with atomic nuclei in the Earth's atmosphere. Predictions and measurements of atmospheric neutrino fluxes are summarized in Fig. 1. Low energy (below ~10 GeV) atmospheric muon and electron neutrinos have been observed in underground detectors [3–5]. At higher energies, from 100 GeV to 400 TeV, neutrino telescopes have measured the spectrum of atmospheric ν_μ [6–9]. In this energy range, the flux of ν_e is expected to be lower by about a factor of 20 [10] and has not been observed.

The main component of the atmospheric neutrino spectrum is produced by the decays of $\pi^\pm$ and $K^\pm$. Asymptotically it can be parametrized by $dN_\nu/dE_\nu \propto E_\nu^{-3.7}$, where E_ν is the neutrino energy [11]. Decays of hadrons containing charm and bottom quarks form an

---

[*] Corresponding author: JKiryluk@lbl.gov
[†] also Università di Bari and Sezione INFN, Dipartimento di Fisica, I-70126, Bari, Italy
[‡] NASA Goddard Space Flight Center, Greenbelt, MD 20771, USA

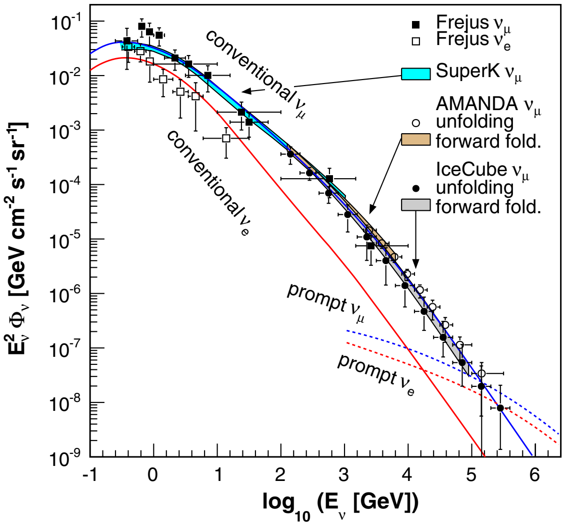

FIG. 1 (color online). Flux predictions for atmospheric muon and electron neutrinos, and measurements of the atmospheric muon neutrino spectrum by Fréjus [4], SuperK [5], AMANDA [6,7], and IceCube [8,9], and of the atmospheric electron neutrino spectrum by Fréjus [4]. Predictions for conventional [27] and prompt [12] atmospheric neutrinos are shown separately. All fluxes are averaged over all arrival directions, include both neutrinos and antineutrinos, and are weighted by E_ν^2 for clarity.

additional component that is expected to be close to the primary cosmic-ray spectrum, $dN_\nu/dE_\nu \propto E_\nu^{-2.7}$ [12–14], and produces nearly equal numbers of ν_μ and ν_e. These prompt neutrinos are expected to dominate the ν_e spectrum at energies above ~30 TeV [10]. The production of ν_τ is expected to be negligible.

Fermi acceleration of charged particles in magnetic shocks followed by collisions with matter or radiation between the source and the Earth naturally leads to an energy spectrum for extraterrestrial neutrinos that is harder than that for atmospheric neutrinos, typically close to $dN_\nu/dE_\nu \propto E_\nu^{-2}$. This allows diffuse extraterrestrial neutrinos to be visible as a hard component to the observed spectrum. The ratio of the ν_e:ν_μ:ν_τ flux in a single astrophysical source depends on the neutrino energy [15]. At moderate (high) energies, the neutrino flavor flux ratio behaves like the one from a pure pion (muon-damped) source, leading to an observed 1:1:1 (1:1.8:1.8) ratio at the Earth after taking into account neutrino oscillations. The energy at which a flavor ratio transition occurs thus depends on the properties of the source [15]. The neutrino flux is not known, although it is expected to be below the Waxman-Bahcall bound [16].

Previous searches for a diffuse flux have been performed with muon neutrinos [11,17], and with cascades [18,19]. Cascades are the particle showers (electromagnetic and hadronic) initiated by charged-current interactions of ν_e and ν_τ and the neutral-current neutrino interactions of all three flavors in a medium. In the charged-current interactions, an average of 80% of the (high-energy) neutrino energy goes into the produced lepton [20]. For ν_e, this leads to an electromagnetic shower, while for ν_τ the character of the lepton-induced shower depends on the τ decay mode. The remainder of the energy is transferred to the target nucleon, producing a hadronic cascade. In the neutral-current interactions, the neutrino transfers a fraction of its energy to the target nucleon producing only a hadronic cascade. A typical cascade deposits its electromagnetic energy in a thin cylinder about 60 cm in diameter and 5 m in length. Hadronic energy is deposited over a larger volume, about 11 m long and 75 cm in diameter. IceCube observes the Cherenkov radiation produced by the charged secondary particles from neutrino-nucleon interactions through an optical sensor array. While a neutrino-induced muon has a tracklike signature in IceCube, a cascade event looks effectively like a point source of Cherenkov light in the detector.

For diffuse searches, cascades from all flavor ν interactions have two advantages over tracks from ν_μ interactions, despite their inherently poor angular resolution compared to muon tracks. The first is that the background from atmospheric neutrinos is lower than for ν_μ. Second, because of their short shower length, the cascades are well-contained in the detector, with a Cherenkov light output proportional to the shower energy, so the shower energy is well measured. The detector acts as a calorimeter. Since the energy spectrum of extraterrestrial neutrinos is expected to be harder than the atmospheric neutrino spectrum, searching for a break in the energy spectrum with cascades is easier than with muons, both due to the expected break being at a lower energy in the cascade channel than the muon channel (a consequence of lower fluxes of atmospheric ν_e than ν_μ), and better intrinsic energy resolution of cascades over muons.

This paper reports on searches for diffuse extraterrestrial and for atmospheric neutrino-induced cascades using 257 days (livetime) of data collected in the year 2007–2008 with a partially completed IceCube detector consisting of 22 of the planned 86 strings. The IceCube detector and data sample are described in Sec. II. Section III describes the analysis. Results are given in Sec. IV, and a summary follows in Sec. V.

II. THE ICECUBE DETECTOR AND DATA SAMPLE

The IceCube detector is composed of vertical strings of optical sensors which are deployed in the glacial ice at the South Pole. The sensors detect Cherenkov radiation from charged particles produced in neutrino interactions. The strings are deployed on a 125 m triangular grid. Each string contains 60 digital optical modules (DOMs), mounted between 1450 and 2450 m below the surface (17 m spacing). Each DOM contains a 10-inch photomultiplier tube (PMT) [21], and a data acquisition system in a pressure vessel. The DOMs are most sensitive to photons with wavelengths 300 to 600 nm. The Hamamatsu R7081-02 PMTs have a peak quantum efficiency of ~25% and are operated at a typical gain of 10^7. The PMT output is linear within 10% up to a current of 50 mA; at a gain of 10^7, this corresponds to 31 detected photoelectrons per nanosecond. The DOM and string performance is described elsewhere [22,23].

The data acquisition system records the arrival times of the detected photoelectrons. It uses two waveform digitization systems which record the arrival time with a time accuracy of about 2 ns and a wide dynamic range [22,24]. One system records data at 300 megasamples/second (MSPS) for 400 ns after the first photon is detected with 14 bits of dynamic range. The second only has 10 bits of dynamic range but records data for 6.4 μs at 40 MSPS. The dead-time of the system is less than 1%. Each DOM is activated (launched) when a single photoelectron is detected, and the data are sent to the surface when two adjacent (nearest or next-to-nearest) neighbors record a hit within 1 μs.

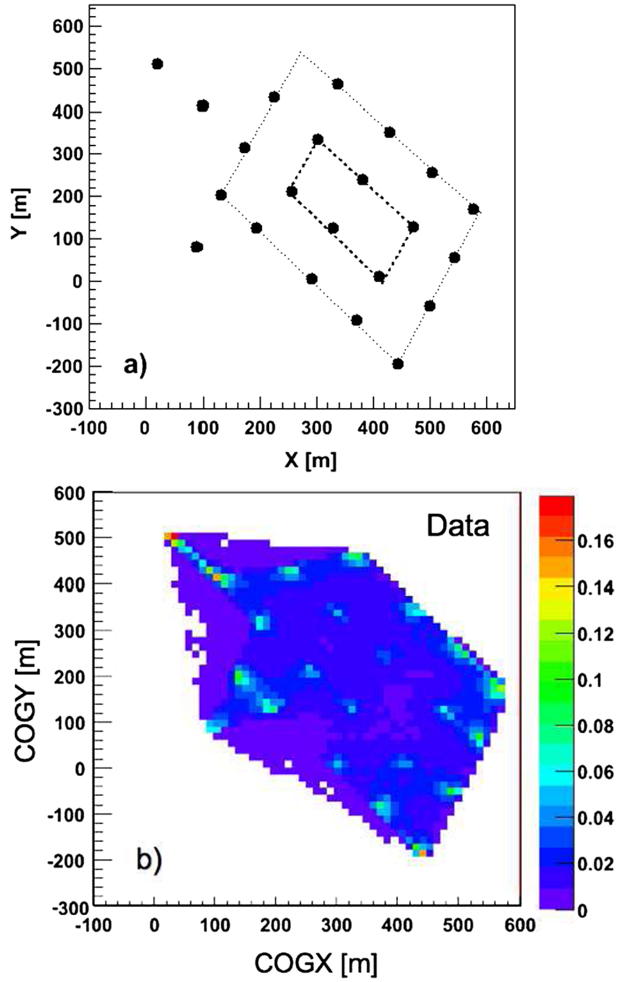

FIG. 2 (color online). a) The filled circles show the positions of the strings in the $x - y$ (horizontal) plane for the 22-string detector configuration. The lines show the boundaries of the fiducial volume and are described in the text. b) The reconstructed center-of-gravity position x (COGX) versus y (COGY) for events passing the cascade online filter. The right axis shows the rate [Hz].

The data were collected between May 2007 and April 2008 when IceCube consisted of 22 active strings with 1320 DOMs. The detector configuration is shown schematically in Fig. 2(a). The point (0,0,0) is the center of the complete 86-string IceCube detector. The main physics trigger was a "simple multiplicity trigger" that required photon signals from at least 8 DOMs, with the additional requirement of accompanying hits in any of the two neighboring DOMs on a string, each above a threshold of 1/6 single photoelectron and within a 5 μs coincidence window. The average trigger rate was ~550 Hz, driven by atmospheric muons, and exhibited about ±10% seasonal variation. Online filters were employed to preselect a data sample for satellite transmission, that was used for analysis.

The online filter relevant to this paper used two first-guess reconstruction algorithms [25]. One algorithm assumed that all hits can be projected onto a line consistent with a particle traveling at a specific velocity. The second algorithm quantified the sphericity of the hit topology. It used the center-of-gravity (COG), defined as the photon signal amplitude weighted mean of all hit DOM positions, as a first-guess vertex position. The response of the algorithms was studied with Monte Carlo simulation. Online selection criteria were developed using these simulations to reject 97.5% of the background events, while retaining 70% of the cascade signal events. The average rate after this filtering was 19 Hz.

III. ANALYSIS

Even after online filtering, the data are dominated by atmospheric muons produced in interactions of cosmic rays with nuclei in the Earth's atmosphere. It is thus necessary to develop stringent offline selections to reject this background while retaining cascade signal events. Two such analyses were performed independently. One analysis focused on cascade events induced by high-energy extraterrestrial neutrino interactions, while the other searched for lower energy atmospheric neutrino-induced cascade signals. The development of the selections for both analyses relies on using 10% of the recorded data while keeping the remaining 90% "blinded." When the selections have been fixed, the 10% sample is discarded and the remaining data is unblinded. The physics results were evaluated from the remaining 90% of the recorded data only after the analysis selections were finalized and were thus free of statistical bias. In addition, extensive Monte Carlo simulations of background and signal events, as well as the IceCube detector response, were used. These simulations used importance sampling and weighting techniques to overcome computing limitations and are described in

Sec. III A. This is followed by a description of the two analyses in Sec. III B. Systematic uncertainties are described in Sec. III C.

A. Monte Carlo simulations

The Monte Carlo generator ANIS [26] was used to generate neutrinos of all flavors in the energy range from ∼10 GeV to 1 EeV at the surface of the Earth and to simulate subsequent neutral and charged-current interactions in the Earth. The neutrino spectra were generated with energy distributions of E^{-2} and E^{-1}, and were reweighted to conventional and prompt atmospheric neutrino flux predictions or to an astrophysical neutrino flux depending on the analysis goal. For the astrophysical neutrino flux we assumed E^{-2} spectrum:

$$E^{-2}\Phi = 5 \times 10^{-7}\ \mathrm{GeV} \cdot \mathrm{cm}^{-2} \cdot \mathrm{s}^{-1} \cdot \mathrm{sr}^{-1} \qquad (1)$$

and the normalization is taken from the final AMANDA upper limit [19]. We modeled the conventional atmospheric fluxes according to the calculations by the Bartol group [27] and the prompt fluxes according to Naumov *et al.* [12] (see Fig. 1). The CTEQ5 parton distribution functions [28] were used in evaluating the neutrino cross-sections. The Preliminary Reference Earth Model [29] was used as the density profile to simulate high-energy neutrino absorption. The simulations included the Glashow resonance $\bar{\nu}_e + e^- \rightarrow W^- \rightarrow X$ for $\bar{\nu}_e$ energies near 6.3 PeV [30].

CORSIKA [31] was used to simulate air showers from cosmic ray collisions in the Earth's atmosphere and obtain a sample of background atmospheric muons. The cosmic ray spectrum was based on the Hörandel polygonato model [32], and primaries up to iron were simulated in the energy range from 600 GeV up to 10^{11} GeV. The SIBYLL parameterization [33] was used in CORSIKA to model hadronic interactions. The effects of the Earth's magnetic field were included in the simulations. By overlaying independent CORSIKA showers, we simulated the coincident muon background, which comes from multiple cosmic-ray showers triggering the detector within its readout window.

High-energy background muons are likely to incur large radiative energy losses, which may mimic cascade signals. To obtain an adequate sample of such high-energy background muons in the simulations, it was necessary to impose additional selections in the CORSIKA event generations. We have imposed threshold selection criteria on the primary cosmic ray energy and on the energy of individual muons, as was done in the AMANDA analysis [19], to increase the effective livetime and Monte Carlo statistics for cosmic rays in the energy range from $\mathcal{O}(10^2)$ TeV to $\mathcal{O}(1)$ PeV. The effective livetimes of these simulation samples are given, together with the threshold values, in Table I for representative cosmic ray energies. The high-energy sample was used only to assess background.

TABLE I. The effective livetimes of the CORSIKA Monte Carlo simulation samples, generated with standard energy thresholds of 600 GeV for primary cosmic-rays and 273 GeV for secondary muons and with high-energy thresholds of 40 TeV and 5 TeV, respectively.

Primary Cosmic Ray Energy	Monte Carlo sample	
	standard [days]	high-energy [days]
10 TeV	1	-
100 TeV	10	50
1 PeV	100	500
10 PeV	1000	5000

A muon Monte Carlo simulator [34] was used to propagate secondary muons through the ice. It simulates muon stochastic energy losses from ionization, bremsstrahlung, photo-nuclear interactions, and pair production.

A cascade Monte Carlo [35] was used to simulate the longitudinal development of electromagnetic and hadronic cascades. It also accounts for the lower Cherenkov light output from hadronic cascades compared to that from electromagnetic cascades.

Cherenkov light emission and subsequent photon propagation through ice was simulated with the Photonics simulation package [36]. In these simulations, the optical properties of the ice were described by a "calibrated ice model." This model was constructed from extensive AMANDA measurements of light propagation in South Pole ice made with artificial *in situ* light sources (pulsed and steady LED sources and nitrogen lasers) [37]. These measurements were largely decoupled from light source and detector characteristics by using timing information of detected single photoelectrons. They determined the relevant wavelength and depth dependences of the optical scattering and absorption lengths, down to the deepest AMANDA depths. Using the fact that scattering and absorption are highly correlated with the concentration of insoluble dust particles in the ice, the model was extrapolated to the greater IceCube depths (from 2100 m down to bedrock at about 2800 m) with dust concentration data from an Antarctic ice core [38], which were scaled to fit the measured scattering and absorption parameters at AMANDA depths. The ice properties are thus less understood at depths greater than 2100 m.

PMT response simulators were used for each DOM in the detector to relate light input and current output. The simulated currents were then propagated through response simulators of the digitization electronics, local coincidence signaling, and event triggering. The same processing and filtering was applied to simulated and recorded data.

B. Event selections

After online filtering and transfer, the data were passed through several maximum-likelihood based reconstruction algorithms [25,39] in order to suppress muon background while retaining signal events. The algorithms assumed a single track, two track, and pointlike cascade hypothesis, and obtained the corresponding vertex positions and times for each event. Following the reconstruction, a sequence of selection criteria was applied to the data. The retained data are identified by different levels, starting from Level-3 (Level-1 refers to triggered online data and Level-2 to the data before offline reconstruction).

At Level-3, only those events were retained for which the single muon track reconstruction found a zenith angle greater than 73°. In addition, a requirement was imposed on the difference of the log-likelihood, $\mathcal{L}$, of the cascade and track reconstructions for each event, $\mathcal{L}(\text{cascade}) - \mathcal{L}(\text{track}) > -16.2$, to preferentially select cascadelike events. The selection criteria were chosen so that the signal efficiency was about 80% in both the atmospheric and extraterrestrial neutrino searches and the muon background rate was reduced by a factor of ~ 5, with respect to the online filter.

Both analyses used the same cascade energy reconstruction algorithm [40] which was applied to events passing Level-3. This analytical cascade-energy calculation takes into account the variation of ice optical properties with depth:

$$E_{\text{reco}}/\text{GeV} = \frac{\sum n_{\text{pe}}}{\sum \mu_0(\vec{r}_v, \vec{r}_{\text{DOM}})}. \tag{2}$$

The n_{pe} is the observed number of photoelectrons in a DOM and $\mu_0(\vec{r}_v, \vec{r}_{\text{DOM}})$ is the number of photoelectrons expected at a given DOM position $\vec{r}_{\text{DOM}}$ from a 1 GeV cascade with a vertex position $\vec{r}_v$. The μ_0 is taken from a table generated by the Photonics Monte Carlo package [36]. In Eq. (2) the noise term has been neglected. It biases the reconstructed energy towards lower values and thus worsens the performance of the cascade energy reconstruction.

The subsequent selections, described below, were optimized separately for the two analyses.

1. Extraterrestrial event selections

Energetic bremsstrahlung from muon tracks outside the detector and muon tracks that intersect only part of the detector can mimic an uncontained cascade signal. To reject this type of background, events were required to have a topology consistent with a cascade signal that originated inside the IceCube instrumented volume at Level-4. Specifically, the four earliest hits in the event were required to be inside the fiducial volume of the detector in the horizontal *x*-*y* coordinates, as depicted in Fig. 2(a) (dotted lines). Events were also rejected if any of the four earliest hits occurred in the eight topmost DOMs. Approximately 5% of the data and 7% of the muon background events from the CORSIKA Monte Carlo remained with respect to the previous selection level. The difference between absolute rates in the data and the CORSIKA Monte Carlo is addressed in Sec. III C. ANIS Monte Carlo simulations show that approximately 13% of the signal was retained at Level-4.

At Level-5, events were required to have hits in at least 20 DOMs. To reject events with multiple muon tracks within the IceCube readout window, an upper limit of 5 μs was set on the event duration, defined as the time difference between the last and the earliest hit in the event. A two-track reconstruction was performed on the retained events and the tracks were required to coincide to within 1 μs. The center-of-gravity of the hits and the vertex coordinates from the cascade reconstruction algorithm were required to coincide in x and y to within 60 m. Monte Carlo simulation studies indicate that these selections reduce the coincident muon rate to less than 20% of the 8 mHz expected background muon rate at level 5.

The smaller event sample allowed for the use of more CPU-intensive reconstruction algorithms. At Level-6, the single-track reconstruction was iterated 32 times with

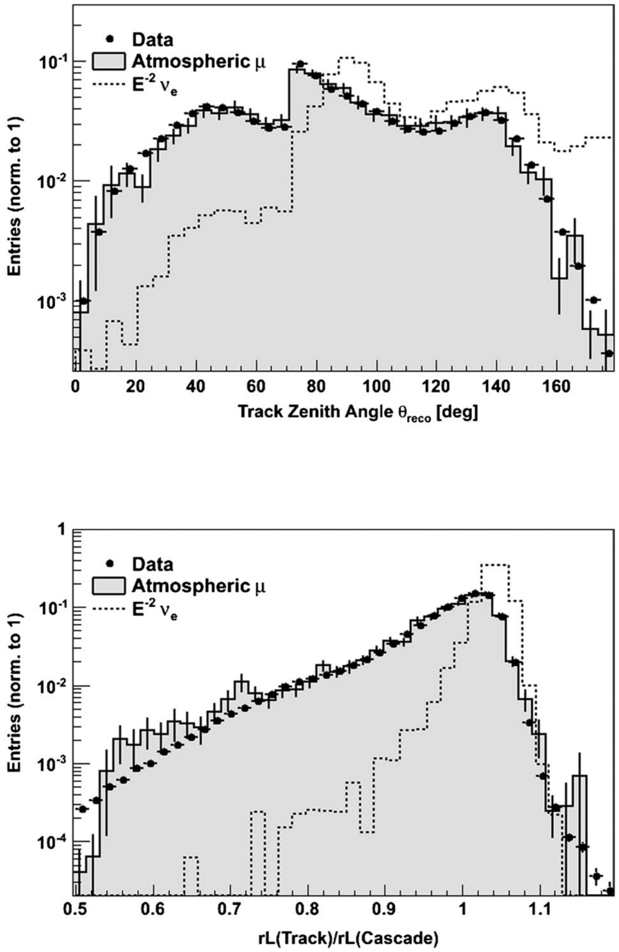

FIG. 3. Normalized distributions of (top) zenith angle and (bottom) reduced log-likelihood ratios after Level-5 event selections for the data (filled circles), muon background Monte Carlo (continuous histogram) and signal neutrino (dashed histogram).

TABLE II. Event rates at different selection levels for the extraterrestrial and atmospheric analyses, described in the text, for the data and for Monte Carlo simulations of atmospheric background muons and of atmospheric and astrophysical neutrinos. An astrophysical neutrino flux of $E^2\Phi = 5.0 \times 10^{-7}$ GeV $\cdot$ cm^{-2} $\cdot$ s^{-1} $\cdot$ sr^{-1} [19] was used for all ν flavors. The atmospheric neutrino fluxes include both a conventional [27] and a prompt [12] component. The statistical uncertainties in the event rates are smaller than 10%.

Selection level		Observed Rate 90% Data [Hz]	Simulated Rate μ [Hz]	$\nu_e^{\rm atm}$ [Hz]	$\nu_\mu^{\rm atm}$ [Hz]	$E^{-2}\nu_e$ [Hz]	$E^{-2}\nu_\mu$ [Hz]	$E^{-2}\nu_\tau$ [Hz]
trigger	1	550	565	1.6×10^{-4}	8.8×10^{-3}	6.0×10^{-5}	3.8×10^{-5}	8.0×10^{-5}
online filter	2	19	14	6.4×10^{-5}	3.8×10^{-4}	4.0×10^{-5}	2.7×10^{-5}	5.5×10^{-5}
	3	3.7	3.0	5.2×10^{-5}	5.7×10^{-5}	3.2×10^{-5}	2.1×10^{-5}	4.5×10^{-5}
Extraterrestrial			Background			Signal		
	4	2.6×10^{-1}	1.5×10^{-1}	1.2×10^{-5}	7.5×10^{-5}	1.2×10^{-5}	6.8×10^{-6}	1.4×10^{-5}
	5	2.1×10^{-2}	8.3×10^{-3}	3.7×10^{-6}	3.4×10^{-6}	8.6×10^{-6}	3.1×10^{-6}	1.1×10^{-5}
	6	1.1×10^{-2}	4.1×10^{-3}	3.3×10^{-6}	2.9×10^{-6}	8.2×10^{-6}	2.8×10^{-6}	1.0×10^{-5}
Atmospheric			Background	Signal				
	4	3.1×10^{-3}	1.8×10^{-3}	1.3×10^{-6}	1.5×10^{-6}	-	-	-

randomly selected seed tracks to ensure that the final reconstructed tracks did not originate from local minima. The zenith angle distribution is shown in the top part of Fig. 3. The selection on zenith angle was refined to reject events with a reevaluated single-track zenith angle smaller than 69°. The comparison of the event reconstruction probabilities with a single-track and a cascade hypothesis was revisited as well. Only those events for which the ratio of the reduced log-likelihood, $r\mathcal{L}$, for the event reconstruction under a single-track and under a cascade hypothesis was greater than 0.95 were retained for further analysis. The $r\mathcal{L}$ is defined as the negative log-likelihood normalized by the number of degrees of freedom. The normalized distribution of the track and cascade reduced likelihood ratio is shown in the bottom part of Fig. 3. The Monte Carlo describes the shapes of experimental data distributions very well. The rates observed in the data and obtained from simulations are given in Table II and discussed in section III C.

Figs. 4 and 5 (top) show comparisons between the Monte Carlo and the data for the cascade reconstructed vertex positions, and the reconstructed energy after Level-6 selections. The shapes agree very well, except vertex position z at the largest depths of the detector where the ice properties are not well described by our simulations. The contribution from the Glashow resonance is clearly visible near the reconstructed cascade energy $\log_{10}(E_{\rm reco}/{\rm GeV}) \sim 6.5$. The reconstructed energy for these and other high-energy cascades that are not contained in the detector is slightly lower than their true energy. Figure 5 (bottom) shows the absolute event rate as a function of primary cosmic-ray energy for the standard and high-energy optimized CORSIKA Monte Carlo after Level-6 event selections with an additional selection criterium on the reconstructed cascade energy of 6.3 TeV. Since the two spectra are consistent within uncertainties, at Level-7 we use the high-energy optimized CORSIKA Monte Carlo.

In order to further distinguish between signal-like and muonlike events, at Level-7 we used the multiplicity and spatial distribution of the hit DOMs. For every event we calculated the distances between each hit DOM and the reconstructed cascade vertex. Event-by-event, the mean distance, D, was evaluated and used as the half-radius in determining fill-ratio F, defined as a fraction of hit DOMs

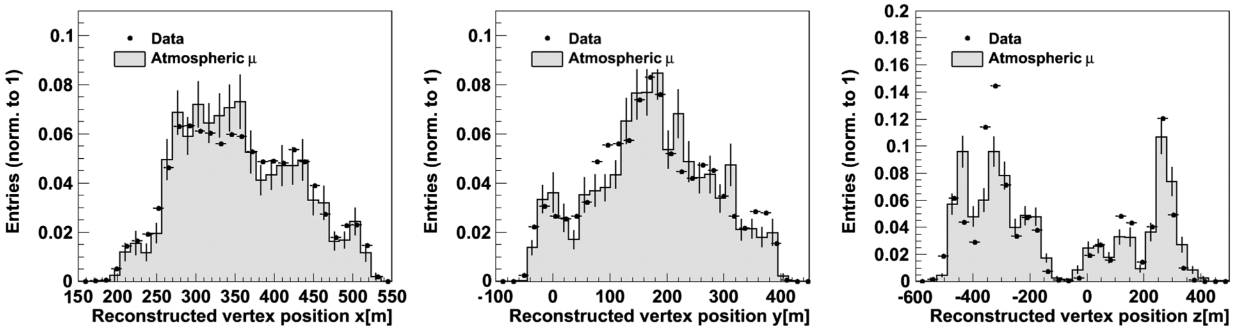

FIG. 4. Normalized distributions of cascade reconstructed vertex position: x component (left panel), y component (middle panel) and z component (right panel) after level-6 event selections for the data (filled circles), standard muon background Monte Carlo (continuous histogram).

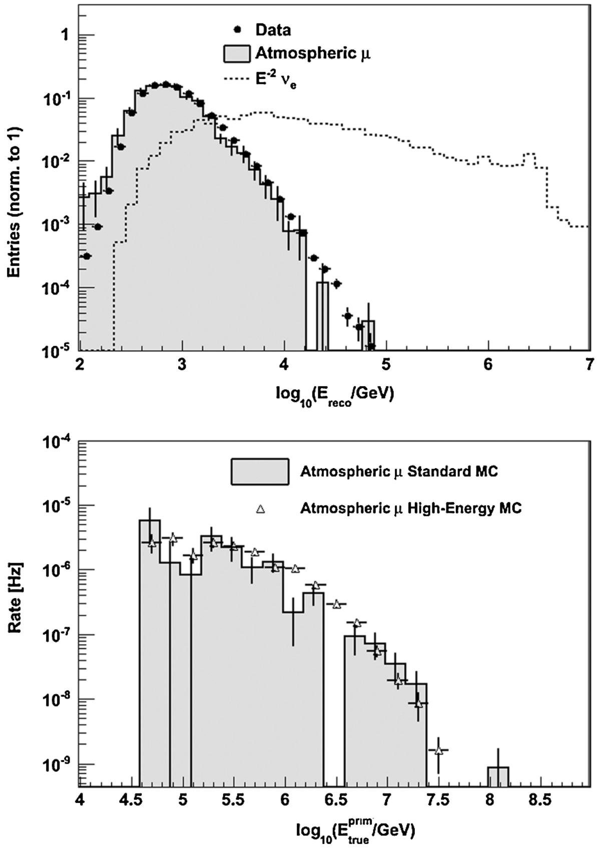

FIG. 5. (top) Normalized distribution of the reconstructed cascade energy after level-6 event selections for the data (filled circles), muon background Monte Carlo (continuous histogram) and signal neutrino (dashed histogram). (bottom) Absolute event rate versus primary cosmic ray energy after level-6 event selections with an additional selection criterium on the reconstructed cascade energy of 6.3 TeV for the standard CORSIKA Monte Carlo (continuous histogram) and high-energy optimized CORSIKA Monte Carlo (open triangles).

within a sphere centered on the cascade vertex for the event. Monte Carlo studies of signal and background exhibit different correlations of D and F, as shown in Fig. 6. For signal-like events, the average F value (sphere density) increases as a function of D, while the opposite is true for the single muon events. Most of coincident muon events have very small values of F, independent of D. Figure 6 also shows the distribution of D and F in the data and Monte Carlo simulations. The background Monte Carlo is in good agreement with the data for the events with the cascade reconstructed vertex position $z > -300$ m as shown in Fig. 6 (bottom-right panel). This is not the case for the events with the cascade reconstructed vertex position $z < -300$ m, where the ice is less well understood and makes some muons look like noncontained cascades (spherical shape and high DOM multiplicity). The muon background events were removed by increasing a threshold on the minimum number of hit DOMs to 60 and imposing a threshold $E_{\text{reco}} > 16$ TeV on the reconstructed cascade energy. These selections also suppress contributions from atmospheric neutrinos from pion and kaon decays. After all selections, four events in the muon background simulation samples and no events in the 10% of the data remained [41].

2. *Atmospheric neutrino event selection*

The atmospheric neutrino analysis used artificial neural networks implemented in the ROOT TMVA package [42] to reject background. The neural networks had two hidden layers, the first with $N + 1$ neurons and the second with N neurons, where N is the number of discriminating variables.

At Level-4, five input variables were used; the track zenith angle of the 32-fold iterative muon reconstruction, the reduced likelihood parameter from the cascade vertex reconstruction, the number of DOMs that register a single photoelectron divided by the total number of photoelectrons seen by all DOMs, the number of direct, unscattered photons assuming a point source at the reconstructed cascade vertex, and the difference in z vertex positions when the cascade vertex is reconstructed using only the earliest registered hits and using only the latest registered hits for the so-called split cascade reconstructions. Figure 7 shows the classification score, Q_A, of the neural network trained from these variables. Only events with $Q_A > 0.4$ were retained. In addition, the reconstructed cascade was required to have an energy larger than 2 TeV and be contained within the detector by imposing an upper value of 1.4 on the parallelogram distance, α, of its horizontal vertex position. The six innermost strings span a parallelogram in x and y, whose edges define $\alpha \equiv 1$. The neighboring strings span a stretched parallelogram with $\alpha = 2$. Parallelograms of $\alpha = 1$ ($\alpha = 2$) are shown as dashed (dotted) lines in Fig. 2(a)]. The containment selection criterium $\alpha < 1.4$ thus requires the vertex to lie at least 75 m from the edge of the detector. With these selections, background was reduced by a factor of 1700 and 2.4% of the signal events were retained.

At Level-5, we chose to train two individual neural networks separately because of limited remaining statistics in the Monte Carlo training samples and to achieve adequate performance. The first neural network was trained with the number of direct hits from the reconstructed cascade vertex, the total number of observed photoelectrons in all DOMs, the difference between log-likelihoods from the cascade vertex reconstruction and from the 32-fold iterative muon track reconstruction, and the reconstructed cascade energy. These four variables correlate in a complex way that merits the use of a neural network. The second neural network was trained with six variables: the distance from the cascade vertex to the first hit in the event, the fill-ratio F, the reduced log-likelihood parameter from the cascade vertex reconstruction, the difference in z vertex positions for the two split cascade reconstructions, the

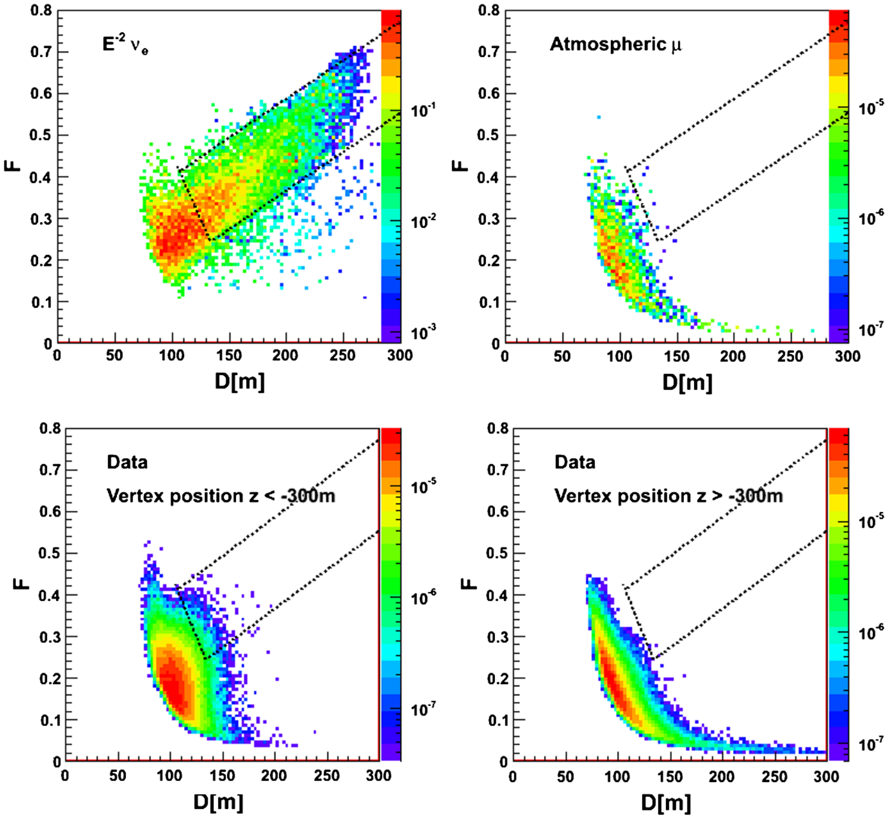

FIG. 6 (color online). The fill-ratio, F, versus the distance, D, as defined in the text for (top-left panel) the Monte Carlo simulated signal sample, (top-right panel) the Monte Carlo simulated muon background sample, and the data at the bottom part of the detector (bottom-left panel) and at the top part of the detector (bottom-right panel). The right axis shows the rate [Hz]. The dashed lines show the selection boundaries applied at Level-7 in the analysis.

track zenith angle of the 32-fold iterative muon reconstruction, and α defined and used before at Level-4. Figs. 8 and 9 show the distributions of selected input variables, whereas Fig. 10 shows the two neural network classification scores Q_B and Q_C.

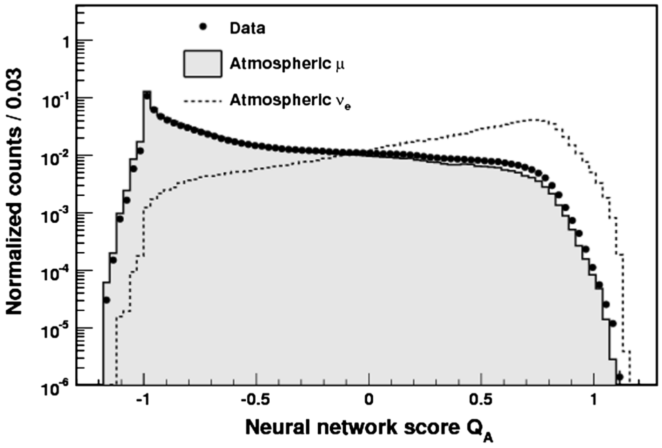

FIG. 7. Normalized distributions of the Level-4 neural network classification score.

The three neural network classification scores, Q_A, Q_B and Q_C were optimized for $E_{reco} > 5$ TeV, and their product, $Q^\star = Q_A \times Q_B \times Q_C$, was used at Level-5. In addition, events with a reconstructed cascade vertex in the topmost 60 meters of the detector were rejected. Multimuon background from coincident cosmic ray air showers was efficiently rejected by a relatively loose selection criterium on the reduced likelihood parameter from the cascade vertex reconstruction. The final selection was $Q^\star > 0.73$ for $E_{reco} > 5$ TeV.

C. Normalization and systematic uncertainties

The extraterrestrial and atmospheric analyses have common sources of systematic uncertainty. The largest contributions to our systematic uncertainty estimate arise from our limited knowledge of the optical properties of the ice and from uncertainties in the cosmic-ray flux and composition. Other significant contributions result from uncertainty in the DOM detection efficiency and from uncertainties in the neutrino cross-sections and the light output from the cascades. These sources affect signal and background estimates differently. We describe signal and background separately below.

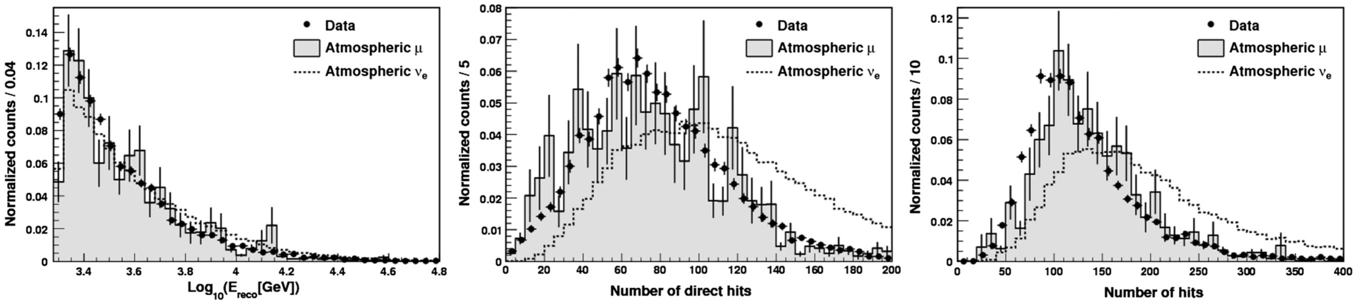

FIG. 8. Normalized distributions (after Level-4 atmospheric selections) of (left panel) reconstructed energy (middle panel) number of direct hits (right panel) total number of hits.

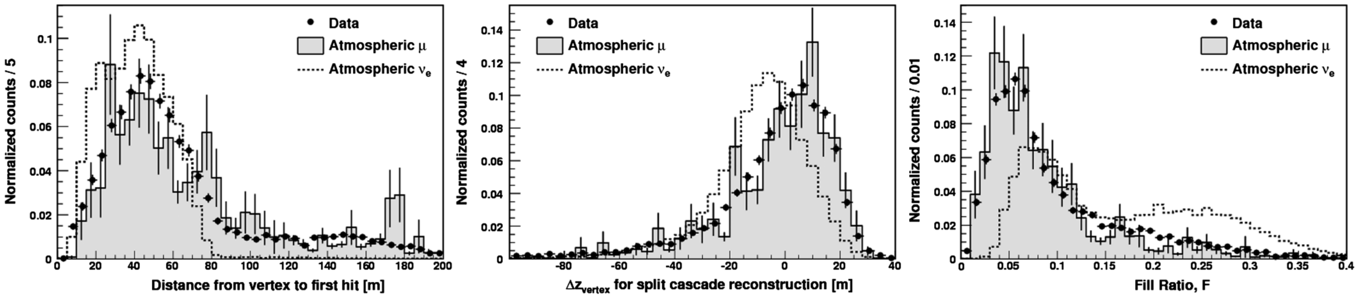

FIG. 9. Normalized distributions (after Level-4 atmospheric selections) of (left panel) distance from the cascade vertex to the first hit in the event (middle panel) difference in z vertex positions for the two split cascade reconstructions (right panel) fill-ratio from the mean hit distance.

1. Muon background systematics

CORSIKA Monte Carlo simulations adequately reproduce the shape of the observed spectra in both analyses but systematically underestimate the absolute rate. In the extraterrestrial analysis, an empirical factor to normalize the rate of simulated background to the corresponding data at the highest selection levels in the analysis was found to be 3 ± 1. Its central value and the uncertainty were determined conservatively by examining the rates as a function of selection level and the reconstructed cascade energy. Background events outnumber signal events by at least 3 orders of magnitude in these event samples. In the atmospheric analysis, the same factor 3 ± 1 was found for $Q^\star < 0.4$, where any cascade signal is expected to be vanishingly small. The factor was the same, within uncertainties, at larger $Q^\star$ values.

Simulations based on an alternate ice model [43] were performed to assess the possible effects on the empirical normalization factor caused by incomplete description of the optical ice properties and necessary approximations in their implementation in the simulations. The alternate model is based on a global fit to recorded charges in very bright events generated by IceCube LED sources sampling all detector depths. The background rates simulated with the alternate ice model differed from the rates observed in the data by a factor of 2. This is consistent, to within the assigned uncertainties, with the difference between the rates simulated using the calibrated ice model and those observed in the data.

The remaining difference in simulated and observed rate is ascribed to the combined effect of uncertainties in the cosmic ray flux for protons in the energy range near the knee, the description of radiative energy losses and in the absolute energy scale.

2. Neutrino systematics

Simulations show that the neutrino event rates are less affected by the ice model than the muon event rates primarily because of differences in the event topologies. We estimate a 20% uncertainty in the rates by comparing simulations with the calibrated and alternate ice models for both atmospheric and E^{-2} energy spectra.

The uncertainty in the DOM sensitivity is taken as 8%, based on the measured uncertainty in the PMT sensitivity [21]. For an E^{-2} neutrino energy spectrum, coupled with a neutrino interaction probability that scales with E, this is equivalent to a 8% uncertainty in flux. For atmospheric neutrinos, the spectrum can be approximated by $E_\nu^{-3.7}$ for conventional neutrinos and by $E_\nu^{-2.7}$ for prompt neutrinos from charm and bottom quark decays. These lead to uncertainties of 20% and 12%, respectively, for the detector sensitivity. We conservatively use the larger value for all atmospheric neutrinos.

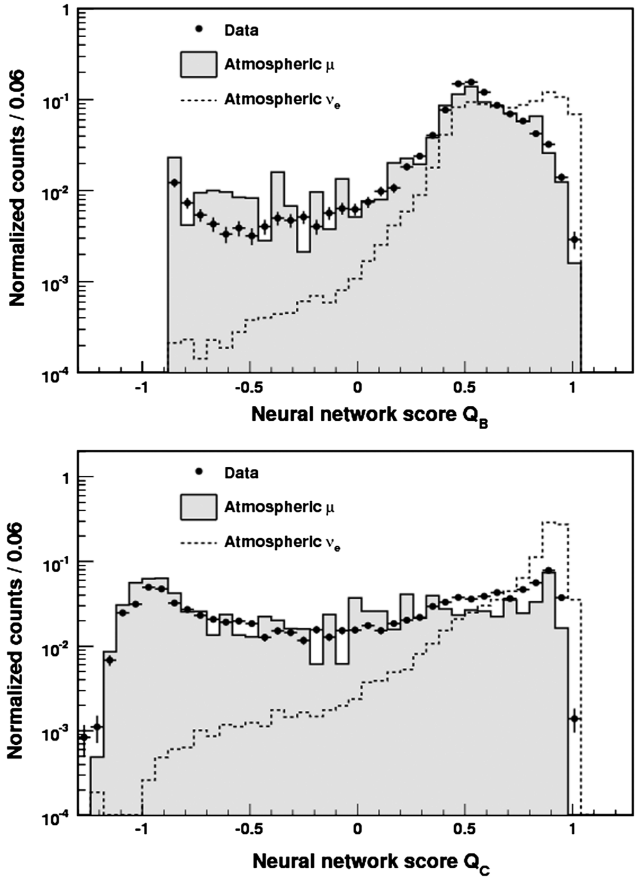

FIG. 10. Normalized distributions of the neural network classification scores (top) Q_B and (bottom) Q_C.

Uncertainty in the atmospheric neutrino flux forms an additional uncertainty in the atmospheric neutrino background to the extraterrestrial cascade search. We assign a 20% uncertainty in these rates [19] to the expected rates of conventional [27] and prompt [12] atmospheric neutrinos.

In the relevant energy range, uncertainty in the neutrino interaction cross-sections is about 6%, caused largely by uncertainties in the parton densities [44,45].

The total uncertainty in the atmospheric (extraterrestrial) neutrino detection efficiency was estimated to be 29% (22%) by adding these contributions in quadrature, see Table III.

To check the energy scale, we studied the detector response to a 337 nm N_2 laser, known as the standard candle. This laser is on one of the IceCube strings, at a depth of 2153 m. It produces light that is shaped like a Cherenkov cone pointing downward; the light output is calibrated to ±10%. For DOMs that are far enough from the laser to avoid saturation (defined as observing less than 20 000 photoelectrons), the total observed charge is 3% lower than our Monte Carlo prediction for the calibrated ice model, and 12% lower than the expectation for the alternate ice model. This is well within the expectations from the ice model and the DOM efficiency uncertainty.

TABLE III. Table of relative systematic uncertainties for the atmospheric and extraterrestrial signal neutrino detection efficiency.

Source	ν^{atm}	$\nu(E^{-2})$
Ice Properties	20%	20%
DOM Efficiency	20%	8%
Neutrino Cross-Section	6%	6%
Total Uncertainty	29%	22%

IV. RESULTS

The data used to develop the selections were discarded prior to evaluating the results. The remaining 90% of the data correspond to 257 days of livetime.

The effective area A_{eff}, defined as the equivalent area with 100% neutrino interaction probability and detection efficiency, was obtained by passing simulated signal Monte Carlo events through the analyses. Figure 11 shows A_{eff} for ν_e, ν_μ, and ν_τ versus neutrino energy. The contribution from the Glashow resonance is clearly visible in A_{eff} for ν_e at trigger level and at final selection level for the extraterrestrial analysis. The analyses cover complementary energy ranges, with the atmospheric analysis naturally covering lower energies than the extraterrestrial analysis. The analyses have similar A_{eff} in the region of overlap.

The energy resolution is $\Delta(\log_{10} E_\nu) \sim 0.26(0.18)$ for the E^{-2} (atmospheric) ν_e energy spectrum. The x, y and z position resolution is ~10 meters.

A. Atmospheric neutrino results

Before unblinding, the event selection criteria for the atmospheric analysis were optimized for a conventional atmospheric neutrino flux with a 5 TeV threshold on the reconstructed cascade energy. Twelve events remained in the 90% of the recorded data after an *a posteriori* selection criterium on the multivariate selection variable $Q^\star$ at 0.9. The expected atmospheric electron and muon neutrino signal is 7.0 ± 2.0 events for these selection criteria. The prompt neutrino component is 25% of the expectation. This signal estimate is based on simulations of conventional [27] and prompt [12] flux predictions as shown in Fig. 1. Only one standard CORSIKA Monte Carlo event passed the final selections. Muon background estimate based on this one Monte Carlo event is 9 ± 9. It includes an empirical scaling factor to normalize the simulated background to the data. The limited background Monte Carlo statistics preclude detection of a signal.

Figure 12 shows the distribution of the variable $Q^\star$ for the full data set with $E_{\text{reco}} > 5$ TeV and compares it to the corresponding distribution for a simulated signal of cascades from atmospheric electron and muon neutrinos.

Figure 13 shows the cumulative number of events as a function of the threshold applied on the $Q^\star$ variable. The top panel compares the experimental data to the signal

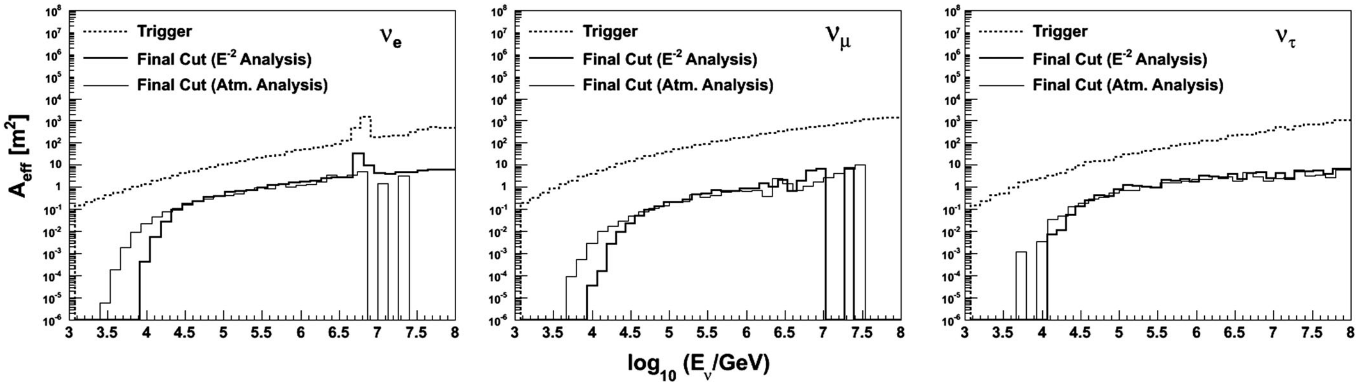

FIG. 11. The effective area, A_{eff}, for (left panel) ν_e, (middle panel) ν_μ, and (right panel) ν_τ versus neutrino energy at trigger level (dashed curves) and at analysis level after all selections for both the extraterrestrial and the atmospheric analysis (continuous curves).

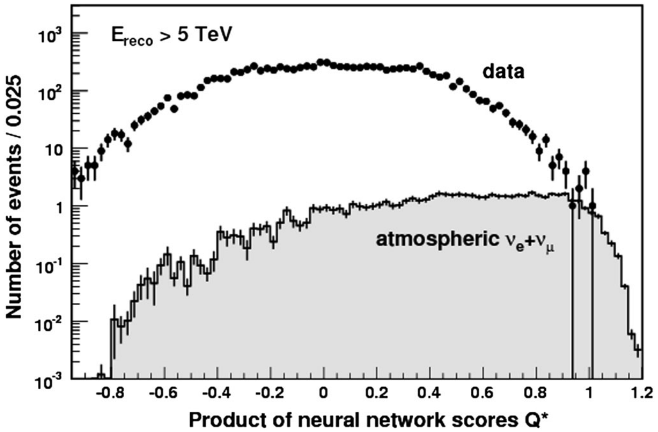

FIG. 12. Distribution of the multivariate selection parameter Q* for data and for a simulated cascade signal from ν_e and ν_μ with reconstructed energies above 5 TeV in the atmospheric analysis.

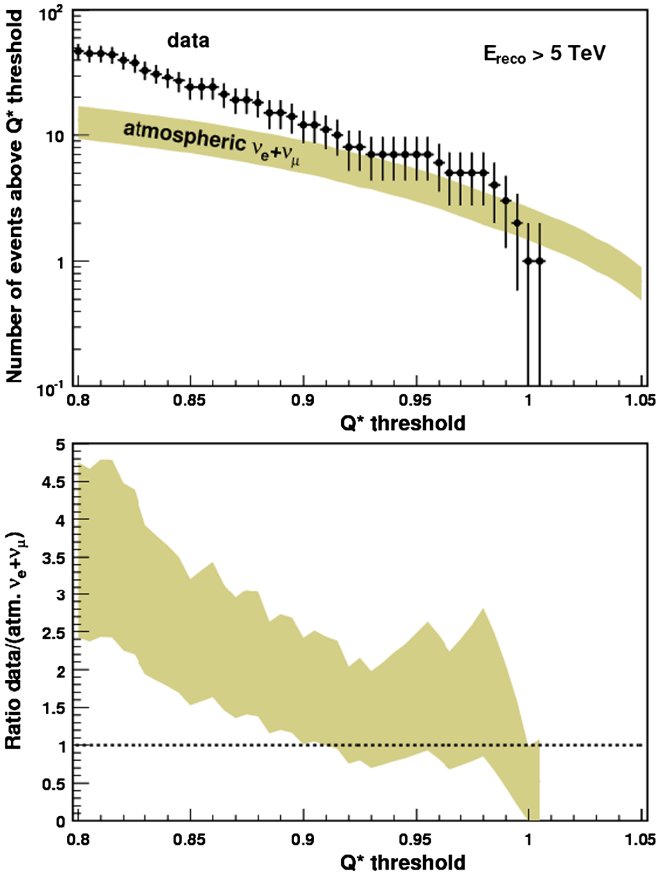

FIG. 13 (color online). Experimental events reconstructed with energies above 5 TeV in the atmospheric analysis compared to an expected cascade signal from atmospheric neutrinos. (top) The cumulative number of events above a threshold in the multivariate selection parameter Q* for data and simulated signal. (bottom) The ratio of data to expected signal as a function of selection threshold.

expectation from simulations, shown as a band with a width determined by the systematic uncertainty in the atmospheric neutrino flux. The bottom panel in Fig. 13 shows the ratio of data events over expected signal events as a function of selection threshold. This ratio crosses unity for the most discriminating selection criterium that can be applied without rejecting all the data, and where the remaining few events have the highest probabilities of being due to atmospheric neutrino cascades. This implies that, in using this analysis, the detector becomes sensitive to atmospheric cascade events due to neutrinos, but the exposure is not sufficient for a statistically significant detection.

At a 15 TeV energy threshold and an a-posteriori selection criterium on the multivariate selection variable $Q^\star > 0.9$, six events remained in the 90% of the recorded data. The expected background from atmospheric muons was estimated to be 5.0 ± 3.8 events. This estimate was made with high-energy CORSIKA simulations and includes the empirical scaling factor to normalize the simulated background to the data. The expected atmospheric electron and muon neutrino signal is 3.0 ± 0.9 events for these selection criteria. The prompt neutrino component is 40% of the expectation. The observed number of events is compatible with Monte Carlo prediction.

B. Diffuse flux limit

The expected number of signal neutrino events and background events after all selections levels in 257 days of livetime was evaluated from Monte Carlo simulations.

The expected number of signal neutrino events was determined for a flux of $E^2\Phi = 5.0 \times 10^{-7}$ GeV $\cdot$ cm^{-2} $\cdot$ s^{-1} $\cdot$ sr^{-1} [19] for all neutrino flavors combined and for the effective areas, A_{eff}, given in Fig. 11. A total of 23 ± 5 signal events is expected with the assumption that the flux receives equal contributions from all flavors. That is, the ν_e:ν_μ:ν_τ flux is 1:1:1 at the Earth. Electron neutrinos contribute about 40%, tau neutrinos about 45% and muon neutrinos the remaining 15% to this event estimate. The expected energy distributions are shown as histogram curves in Fig. 14.

The expected number of background events after all selections levels amounts to 8.3 ± 3.6 events, consisting of atmospheric muon and atmospheric neutrino contributions. Four simulated events from the high-energy CORSIKA Monte Carlo background sample satisfy all event selection criteria. They all originated from proton induced showers, with zenith angles of around 70 degrees and energies in the range of 0.5–3.5 PeV. Figure 16 shows an event display for one of these four Monte Carlo muon background events. The four simulated events that satisfied all selections correspond to 5.4 ± 3.5 muon background events in 257 days of livetime, after the event weights in the simulation and the rate normalization were taken into account. The number of background atmospheric neutrinos from conventional and prompt sources was estimated to be 2.9 ± 0.9, where the central value of 2.9 was obtained assuming atmospheric neutrino fluxes from Refs. [12,27].

The discovery potential of the measurement, defined as the strength of a diffuse astrophysical neutrino flux with an E^{-2} energy spectrum that is needed to obtain a 5σ discovery at 90% confidence level [46] in 257 days of livetime, was estimated after the event selections had been finalized and before the analyses were unblinded. This strength is 5.5×10^{-7} GeV $\cdot$ cm^{-2} $\cdot$ s^{-1} $\cdot$ sr^{-1} in the simulated neutrino energy range from 24 TeV to 6.6 PeV, corresponding to 25 signal events. The flux sensitivity, defined as the average 90% upper limit obtained for a set of hypothetical experiments with no true signal [47] in 257 days of livetime, is 2.0×10^{-7} GeV $\cdot$ cm^{-2} $\cdot$ s^{-1} $\cdot$ sr^{-1}, in the same

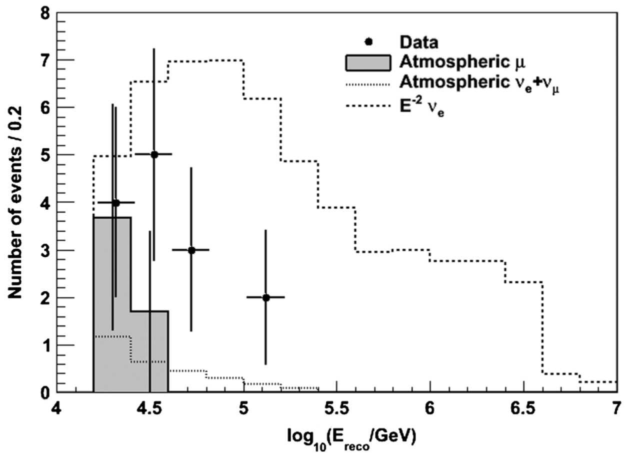

FIG. 14. Cascade reconstructed energy distribution after all selections in the extraterrestrial analysis.

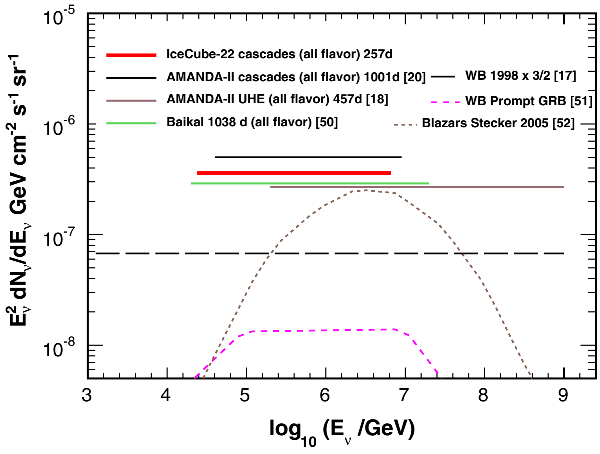

FIG. 15 (color online). Experimental upper limits on the diffuse flux of neutrinos from sources with $\Phi \propto E^{-2}$ energy spectrum and theoretical predictions for neutrino fluxes from astrophysical neutrino sources.

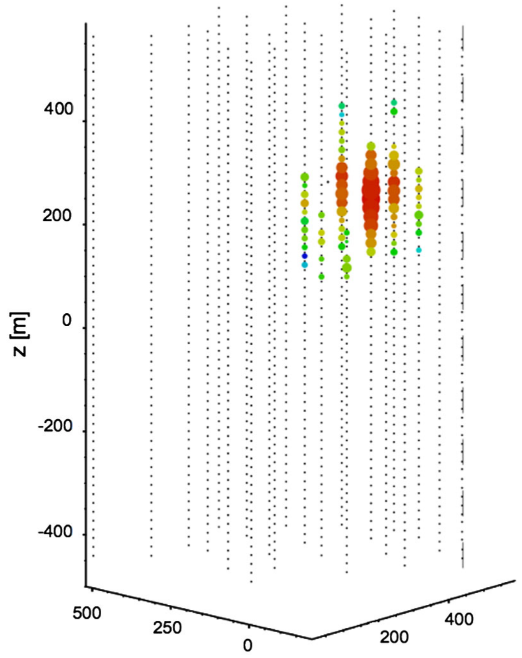

FIG. 16 (color online). The MC muon background event which passed all selections in extraterrestrial analyses and which has the reconstructed energy of 18 TeV is displayed from the side. Different colors of the circles represent different DOMs hit times, with early hits in red and late hits in blue. The size of the circles represents the amplitude.

energy range. All systematic uncertainties have been included in the flux sensitivity calculation.

A total of 14 observed events passed all selection levels in the extraterrestrial data analysis with an expected total background of 8.3 ± 3.6 events. By using the Feldman-Cousins method [48] as implemented in the software package POLE++ [49] to account for statistical and systematic uncertainties in the estimated background and signal counts, we set an upper limit on the number of signal events at 90% confidence level of $\mu_{90\%} = 16.6$.

This upper limit of 16.6 events is below the discovery threshold of 25 signal events. In the absence of signal, we set an upper limit at 90% confidence of $E^2\Phi_{90\%\mathrm{C.L.}} < 3.6 \times 10^{-7}\ \mathrm{GeV} \cdot \mathrm{cm}^{-2} \cdot \mathrm{s}^{-1} \cdot \mathrm{sr}^{-1}$ on the diffuse flux of neutrinos of all flavors assuming that $\Phi \propto E^{-2}$ and that the flux at the detector receives equal contributions from all flavors.

An upper limit on the flux of ν_e that does not depend on the assumption of equal flux contributions for each flavor was derived by assuming that the ν_μ and ν_τ fluxes are zero. This upper limit on the flux of electron neutrinos is $E^2\Phi_{90\%\mathrm{C.L.}} < 3.0 \times 10^{-7}\ \mathrm{GeV} \cdot \mathrm{cm}^{-2} \cdot \mathrm{s}^{-1} \cdot \mathrm{sr}^{-1}$.

In these limits, the central 90% of ν signal events have energies in the range from 24 TeV to 6.6 PeV with a mean energy of ~220 TeV. The limits are shown in Fig. 15.

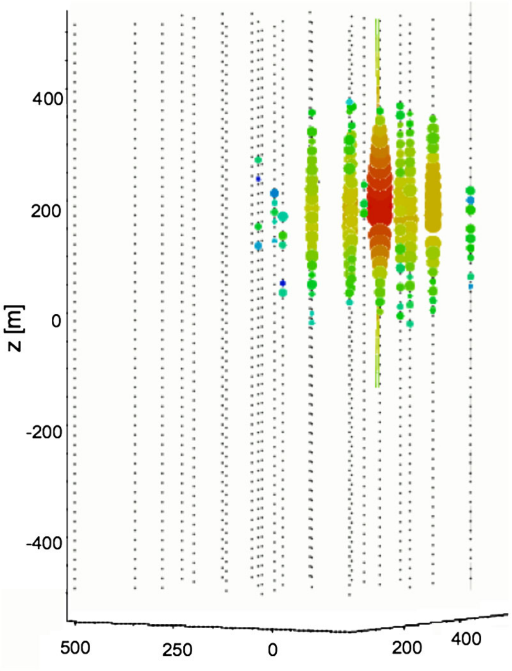

FIG. 17 (color online). The data event which passed all selections in atmospheric and extraterrestrial analyses and which has the highest reconstructed energy of 134 TeV is displayed from the side. Different colors of the circles represent different DOMs hit times, with early hits in red and late hits in blue. The size of the circles represents the amplitude.

Figure 17 shows the experimental event with the highest reconstructed energy that passed all selections in both atmospheric and extraterrestrial analyses.

V. SUMMARY

In summary, we report the first search for cascades induced by atmospheric and by diffuse astrophysical neutrinos with the IceCube detector. The data, obtained in 2007–2008 with a configuration of 22 active strings, amount to 257 days of livetime and were searched for charged-current interactions of ν_e and ν_τ, and for neutral-current interactions of neutrinos of all flavors.

The atmospheric neutrino analysis used neural-network based event selections and resulted in a total of 12 candidate events with energies above 5 TeV after event selections. Within the large uncertainties, the observed number of events is consistent with the expected background.

The astrophysical neutrino analysis used one and two dimensional selection criteria and was optimized for higher energies than the atmospheric neutrino analysis. A total of 14 events with energies above 16 TeV remained after event selections, with an expected total background contribution of 8.3 ± 3.6 events. We derive an upper limit at 90% confidence of $E^2\Phi_{90\%\mathrm{CL}} < 3.6 \times 10^{-7}\ \mathrm{GeV} \cdot \mathrm{cm}^{-2} \cdot \mathrm{s}^{-1} \cdot \mathrm{sr}^{-1}$ on the diffuse flux of astrophysical neutrinos with the assumption that the energy spectrum $\Phi \propto E^{-2}$ and that the flavor composition of the ν_e:ν_μ:ν_τ flux is 1:1:1 at the Earth. In this limit, 90% of the expected signal events have energies between 24 TeV and 6.6 PeV.

This is below the limit that was recently reported from final AMANDA data, corresponding to 1001 days of livetime [19]. IceCube construction has been completed in 2011. The detector consists of 86 strings covering a volume of 1 km^3. Future IceCube searches will thus benefit from a considerably larger size and are expected to have significantly improved detection sensitivity.

ACKNOWLEDGMENTS

We acknowledge the support from the following agencies: U.S. National Science Foundation-Office of Polar Programs, U.S. National Science Foundation-Physics Division, University of Wisconsin Alumni Research Foundation, the Grid Laboratory Of Wisconsin (GLOW) grid infrastructure at the University of Wisconsin—Madison, the Open Science Grid (OSG) grid infrastructure; U.S. Department of Energy, and National Energy Research Scientific Computing Center, the Louisiana Optical Network Initiative (LONI) grid computing resources; National Science and Engineering Research Council of Canada; Swedish Research Council, Swedish Polar Research Secretariat, Swedish National Infrastructure for Computing (SNIC), and Knut and Alice Wallenberg Foundation, Sweden; German Ministry for Education and Research (BMBF), Deutsche Forschungsgemeinschaft

(DFG), Research Department of Plasmas with Complex Interactions (Bochum), Germany; Fund for Scientific Research (FNRS-FWO), FWO Odysseus programme, Flanders Institute to encourage scientific and technological research in industry (IWT), Belgian Federal Science Policy Office (Belspo); University of Oxford, United Kingdom; Marsden Fund, New Zealand; Japan Society for Promotion of Science (JSPS); the Swiss National Science Foundation (SNSF), Switzerland; A. Groß acknowledges support by the EU Marie Curie OIF Program; J. P. Rodrigues acknowledges support by the Capes Foundation, Ministry of Education of Brazil.

[1] F. Halzen, AIP Conf. Proc. No. 1182 (AIP, New York, 2009).
[2] R. Abbasi *et al.*, Astrophys. J. **701**, L47 (2009); Phys. Rev. D **79**, 062001 (2009); A. Achterberg *et al.*, Phys. Rev. D **75**, 102001 (2007).
[3] for a review see e.g. M. C. Gonzalez-Garcia and Y. Nir, Rev. Mod. Phys. **75**, 345 (2003), and references therein.
[4] K. Daum *et al.*, Z. Phys. C **66**, 417 (1995).
[5] C. Gonzalez-Garcia, M. Maltoni, and J. Rojo, J. High Energy Phys. 10 (2006) 075.
[6] R. Abbasi *et al.*, Phys. Rev. D **79**, 102005 (2009).
[7] R. Abbasi *et al.*, Astropart. Phys. **34**, 48 (2010).
[8] R. Abbasi *et al.*, Phys. Rev. D **83**, 012001 (2011).
[9] R. Abbasi *et al.*, arXiv:1104.5187 [Phys. Rev. D (to be published)].
[10] J. F. Beacom and J. Candia, J. Cosmol. Astropart. Phys. 11 (2004) 009.
[11] A. Achterberg *et al.*, Phys. Rev. D **76**, 042008 (2007).
[12] G. Florentini, A. Naumov, and F. L. Villante, Phys. Lett. B **510**, 173 (2001).
[13] R. Enberg, M. H. Reno, and I. Sarcevic, Phys. Rev. D **78**, 043005 (2008).
[14] A. D. Martin, M. G. Ryskin, and A. M. Stasto, Acta Phys. Pol. B **34**, 3273 (2003).
[15] T. Kashti and E. Waxman, Phys. Rev. Lett. **95**, 181101 (2005).
[16] E. Waxman and J. Bahcall, Phys. Rev. D **59**, 023002 (1998); J. Bahcall and E. Waxman, Phys. Rev. D **64**, 023002 (2001).
[17] M. Ackermann *et al.*, Astrophys. J. **675**, 1014 (2008).
[18] J. Ahrens *et al.*, Phys. Rev. D **67**, 12003 (2003); M. Ackermann *et al.*, Astropart. Phys. **22**, 127 (2004).
[19] R. Abbasi *et al.*, Astropart. Phys. **34**, 420 (2011).
[20] R. Gandhi *et al.*, Astropart. Phys. **5**, 81 (1996).
[21] R. Abbasi *et al.*, Nucl. Instrum. Methods Phys. Res., Sect. A **618**, 139 (2010).
[22] A. Achterberg *et al.*, Astropart. Phys. **26**, 155 (2006).
[23] S. Klein (IceCube Collaboration), IEEE Trans. Nucl. Sci. **56**, 1141 (2009).
[24] R. Abbasi *et al.*, Nucl. Instrum. Methods Phys. Res., Sect. A **601**, 294 (2009).
[25] J. Ahrens *et al.*, Phys. Rev. D **67**, 012003 (2003).
[26] A. Gazizov and M. Kowalski, Comput. Phys. Commun. **172**, 203 (2005).
[27] G. D. Barr, T. K. Gaisser, P. Lipari, S. Robbins, and T. Stanev, Phys. Rev. D **70**, 023006 (2004).
[28] H. L. Lai *et al.*, Eur. Phys. J. C **12**, 375 (2000).
[29] A. Dziewonski, in *The Encyclopedia of Solid Earth Geophysics*, edited by David E. James (Van Nostrand Reinhold, New York, 1989), p. 331.
[30] S. L. Glashow, Phys. Rev. **118**, 316 (1960).
[31] D. Heck *et al.*, Report FZKA 6019 (1998), http://bibliothek.fzk.de/zb/berichte/FZKA6019.pdf.
[32] J. R. Hörandel, Astropart. Phys. **21**, 241 (2004).
[33] E. J. Ahn, R. Engel,T. K. Gaisser, P. Lipari, and T. Stanev, Phys. Rev. D **80**, 094003 (2009).
[34] D. Chirkin and W. Rhode, arXiv:hep-ph/0407075.
[35] B. Voigt, Ph.D. thesis, Humboldt University, Berlin, 2008.
[36] J. Lundberg *et al.*, Nucl. Instrum. Methods Phys. Res., Sect. A **581**, 619 (2007).
[37] M. Ackermann *et al.*, J. Geophys. Res. D **111**, 13203 (2006).
[38] IceCore East Dronning Maud Land, Antarctica (EDML) data.
[39] J. Ahrens *et al.*, Nucl. Instrum. Methods Phys. Res., Sect. A **524**, 169 (2004).
[40] M. D'Agostino, Ph.D. thesis, University of California, Berkeley, 2009, arXiv:0910.2555.
[41] J. Kiryluk (IceCube Collaboration), in Proceedings of the 31st International Cosmic Ray Conference, 2009 (to be published), arXiv:0909.0989v1.
[42] A. Hocker *et al.*, Proc. Sci., ACAT2007 (2007) 040 [arXiv:physics/0703039v5].
[43] D. Chirkin, IceCube Internal Report 200911002, 2009.
[44] A. Achterberg *et al.*, Phys. Rev. D **75**, 102001 (2007).
[45] R. Abbasi *et al.*, Phys. Rev. D **82**, 072003 (2010).
[46] G. C. Hill, J. Hodges, B. Hughey, A. Karle, and M. Stamatikos, in *Proc. of the PHYSTATO5* (Imperial College Press, Oxford, 2005).
[47] G. C. Hill and K. Rawlins, Astropart. Phys. **19**, 393 (2003).
[48] G. J. Feldman and R. D. Cousins, Phys. Rev. D **57**, 3873 (1998).
[49] J. Conrad, O. Botner, A. Hallgren, and C. Perez de los Heros, Phys. Rev. D **67**, 12002 (2003).
[50] A. V. Avrorin *et al.*, Astron. Lett. **35**, 651 (2009).
[51] E. Waxman and J. Bahcall, Phys. Rev. Lett. **78**, 2292 (1997).
[52] F. W. Stecker, Phys. Rev. D **72**, 107301 (2005).